Appl Phys A (2009) 95: 131–138
DOI 10.1007/s00339-008-5032-y

Applied Physics A
Materials Science & Processing

Electronic structure of thin film iron-tetracyanoethylene: $Fe(TCNE)_x$

Pramod Bhatt · E. Carlegrim · A. Kanciurzewska · M.P. de Jong · M. Fahlman

Received: 12 July 2008 / Accepted: 24 November 2008 / Published online: 19 December 2008

Abstract Thin film iron-tetracyanoethylene $Fe(TCNE)_x$, $x \sim 2$, as determined by photoelectron spectroscopy, was grown in situ under ultra-high vacuum conditions using a recently developed physical vapor deposition-based technique for fabrication of oxygen- and precursor-free organic-based molecular magnets. Photoelectron spectroscopy results show no spurious trace elements in the films, and the iron is of Fe^{2+} valency. The highest occupied molecular orbital of $Fe(TCNE)_x$ is located at ∼1.7 eV vs. Fermi level and is derived mainly from the $TCNE^-$ singly occupied molecular orbital according to photoelectron spectroscopy and resonant photoelectron spectroscopy results. The Fe(3d)-derived states appear at higher binding energy, ∼4.5 eV, which is in contrast to $V(TCNE)_2$ where the highest occupied molecular orbital is mainly derived from V(3d) states. Fitting ligand field multiplet and charge transfer multiplet calculations to the Fe L-edge near edge X-ray absorption fine structure spectrum yields a high-spin Fe^{2+} ($3d^6$) configuration with a crystal field parameter $10Dq \sim 0.6$ eV for the $Fe(TCNE)_x$ system. We propose that the significantly weaker Fe-TCNE ligand interaction as compared to the room temperature magnet $V(TCNE)_2$ ($10Dq \sim 2.3$ eV) is a strongly contributing factor to the substantially lower magnetic ordering temperature (T_C) seen for $Fe(TCNE)_x$-type magnets.

PACS 73.20.At · 75.50.Xx · 79.60.Fr

1 Introduction

After the discovery of room temperature magnetism in $V(TCNE)_2 \cdot y$(solvent) [1], a considerable interest has been generated in the field of organic magnets [2], specifically regarding the $M^{2+}(TCNE^-)_2 \cdot y$(solvent) type [3] where M is metal such as V, Mn, Fe, Co, Ni and TCNE = tetracyanoethylene, an organic compound. The advantages of such organic-based magnets compared to conventional magnets are relative light weight, flexibility, and low-cost synthesis. These magnets have numerous potential applications [4–6] and form a unique class of materials which exhibit unusual physical properties. It is proposed that the magnetism in this class of magnets results from antiferromagnetic coupling between the spin from the unpaired electron in the $(TCNE)^- \pi^*$ orbital (hence having spin $S = 1/2$) and the spin in the metal ion, M^{2+} (spin $S = 3/2$ for, e.g., V^{2+}). Besides magnetic ordering, these magnets have semiconducting properties and can be synthesized by chemical routes in the presence of organic solvents. The synthesis produces insoluble powder [3], however, so chemical vapor deposition (CVD) of $M(TCNE)_x$, $x \sim 2$, was recently developed to enable thin film deposition and avoid inclusion of solvents [7–9].

P. Bhatt · E. Carlegrim · M. Fahlman (✉)
Department of Physics, Chemistry and Biology, Linköping University, 58183 Linköping, Sweden
e-mail: mafah@ifm.liu.se

A. Kanciurzewska
Applied Photochemistry Lab, Faculty of Chemistry, Adam Mickiewicz University, 60-780 Poznań, Poland

M.P. de Jong
MESA Institute for Nanotechnology, University of Twente, 7500 AE Enschede, The Netherlands

Present address:
P. Bhatt
Max-Planck-Institut für Metallforschung, Heisenbergstraße 3, 70569 Stuttgart, Germany

Only few organic-based materials exhibit magnetic ordering at or near room temperature, and properties of these magnets/materials are often difficult to reproduce. That is why, among the $M(TCNE)_2$-type magnets, $V(TCNE)_2$ has received much attention due to its magnetic ordering that is well above room temperature ($T_C \sim 400$ K). The powder-based magnets of this class that use other metals, such as Mn, Fe, Co, and Ni, have much lower critical temperature with none exceeding a T_C of 122 K. Depending upon the method of preparation, the magnetic ordering temperature can be altered, however, either by choice of solvent for the powder-form magnets [10, 11] or by excluding the solvents altogether by following the CVD approach [12]. The main problem of this class of magnets in general, and $V(TCNE)_2 \cdot y$(solvent) in particular, is the extreme sensitivity to air [1], which makes them very difficult to study and use much less in applications. Neither the existing powder form synthesis nor the CVD thin film processes developed were compatible with ultra-high vacuum (UHV) in situ fabrication, which would be necessary for studies and devices that involve surface properties. Two new UHV-compatible techniques [13, 14] for in situ deposition of $M(TCNE)_x$-type magnets have been developed, however, that help alleviate these problems. A modified CVD-based technique enabled, for the first time, oxygen-free thin films of $V(TCNE)_2$ to be fabricated and studied, revealing thin film room temperature magnetic ordering [13] and establishing the nature of the highest occupied molecular orbital (HOMO) [13, 15] and lowest unoccupied molecular orbital (LUMO) [16, 17] of $V(TCNE)_2$. It also was shown that the presence of a small amount of contamination and/or disorder in the film not only may affect drastically the magnetic ordering [10–12], as mentioned above, but also the electronic properties of the material [17].

Though the CVD-fabricated films remove solvent-induced disorder, they still may contain defects from the precursors [15, 17] that induce physical disorder and introduce trap states [17]. In order to avoid the precursor-derived defects in the films, we have recently developed a physical vapor deposition (PVD) method for fabricating $M(TCNE)_x$ magnets [14], enabling oxygen- and solvent/precursor-defect-free thin films to be fabricated in situ. In the present paper we have used this PVD-based technique to fabricated thin films of $Fe(TCNE)_x$ magnets in situ at ultra-high vacuum and at room temperature. We present the first electronic structure study of $Fe(TCNE)_x$ using a variety of photoemission and X-ray absorption techniques combined with theoretical modeling. Since magnetism is strongly linked to electronic structure, we expect that the findings will enable a better understanding of the variation in magnetic properties of the $M(TCNE)_x$ class of materials.

2 Experimental and theoretical techniques

$Fe(TCNE)_x$ thin film magnets were prepared in situ by using physical vapor deposition at room temperature. The $Fe(TCNE)_x$ thin films were deposited on clean gold substrates. The base pressure of the preparation chamber was better than 10^{-9} mbar. Photoelectron spectroscopy (PES), resonant photoelectron spectroscopy (RPES), X-ray absorption spectroscopy (XAS), and near edge X-ray absorption fine structure (NEXAFS) spectroscopy were carried out on the in situ fabricated thin films at beam line D1011 at the Max-II storage ring of the MAX-laboratory for Synchrotron Radiation Research in Lund, Sweden. The end station is equipped with a Scienta SES-200 hemispherical electron energy analyzer and has a custom built micro-channel plate (MCP) detector for electron yield measurements (NEXAFS). An incident angle $\theta = 45°$ of the photon beam relative to the sample normal was used for the NEXAFS and PES measurements. Calibration of the photon energies (monochromator) and the SES-200 analyzer was carried out yielding an error of $<\pm 0.1$ eV for the binding energies given in the paper.

The Fe L-edge XAS spectrum was analyzed using ligand field multiplet (LFM) and charge transfer multiplet (CTM) calculations as developed by Thole and co-workers [18–20], based on Cowan's atomic multiplet code and Butler's group theoretical code [21, 22]. In LFM calculations, the interaction with neighboring atoms is taken into account in a simple way by lowering of the ground state symmetry and the introduction of the crystal field, which, for cubic fields, is traditionally parameterized by D_q, D_s, and D_t. In addition, hybridization effects can be modeled by tuning the reduction factor, κ, of the Slater integrals to account for the expansion of the 3d-derived wave functions in case of increasing covalence of the bonds. CTM calculations were used to model possible Fe(3d)-TCNE(π) hybridization in terms of ligand to metal charge transfer (CT). The scheme employs configuration interaction, in which the electronic states are described as a mixture of $3d^n$ and $3d^{n+1}\underline{L}$, where $\underline{L}$ is a ligand hole resulting from π-electron donation to the Fe from the TCNE.

3 Result and discussion

The stoichiometry of the $Fe(TCNE)_x$ films was obtained from survey spectra using atomic sensitivity factors [23], and yielded $x \sim 2.1 \pm 0.2$ No O(1s) core level signal was present in the films, confirming that oxygen-free $Fe(TCNE)_x$ (within the detection limit of $\pm 0.1\%$) were grown. Figure 1 presents core level spectra of C(1s), N(1s), and Fe(2p). The C(1s) peak binding energy of 286.0 eV is the same as for $V(TCNE)_2$ thin films [15, 16], and the N(1s) binding energy

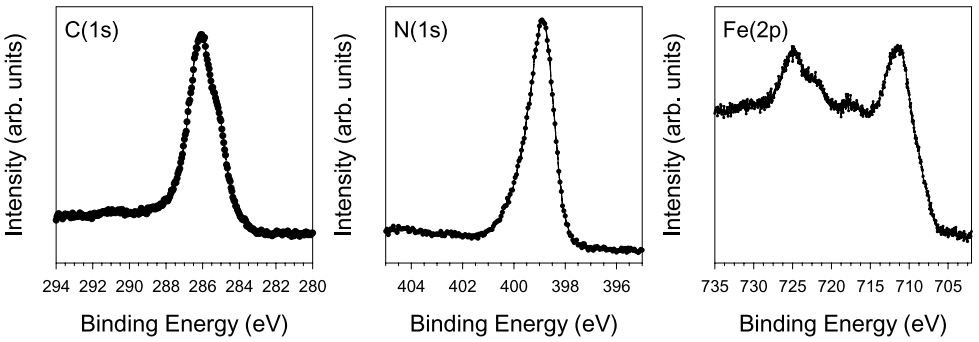

Fig. 1 Core-level spectra of C(1s) (*left*), N(1s) (*center*), and Fe(2p) (*right*) taken at $h\nu = 700$, 800, and 1100 eV, respectively

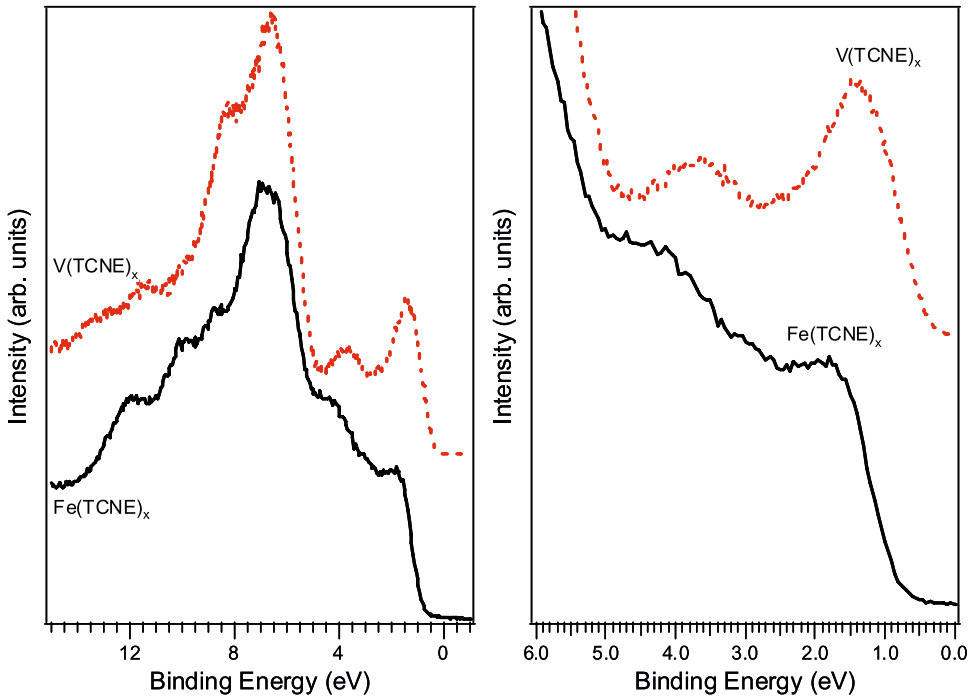

Fig. 2 *Left panel*: valence region spectra of thin film Fe(TCNE)$_x$ (*black, solid line*) and V(TCNE)$_x$ (*red, dashed line*) taken at $h\nu = 100$ eV. Intensity normalized on peak at ~6.7 eV. *Right panel*: expanded frontier valence region

of 398.8 eV is identical to that for V(TCNE)$_2$ [14]. The C(1s) and N(1s) core level peak position, together with the 1:2 Fe:TCNE ratio, thus indicates that the TCNE molecules receive one electron each as is the case for V(TCNE)$_2$. The Fe(2p) core level spectrum confirms chemical interaction of TCNE with Fe as the position of the Fe(2p$_{3/2}$) main peak is shifted ~4.5 eV towards higher binding energy with respect to Fe(2p$_{3/2}$) peak of pure iron metal. The positive shift for Fe(2p) and negative shift for C(1s) and N(1s) peaks all suggest charge transfer from Fe metal to TCNE compound, and based on the estimated stoichiometry of $x \sim 2$, Fe is tentatively assigned as Fe^{2+}.

Figure 2 presents the valence band spectra of Fe(TCNE)$_x$ and, for comparison, V(TCNE)$_x$, $x \sim 2$, taken at 100 eV photon energy. The most intense feature for Fe(TCNE)$_x$ is the broad peak located at 6.7 eV. There are three peaks riding on the high binding energy side slope, located at 8.8, 10.2, and 12.1 eV and three features in the region 1–5 eV. Looking more closely at the frontier occupied valence region for Fe(TCNE)$_x$ displayed in the right panel of Fig. 2, we see a valence edge feature at 1.7 eV that represents the highest occupied molecular orbital. A second feature is located around 3.0 eV, riding on the slope of the third and strongest peak at 4.5 eV. We see no evidence for metallic Fe in the spectra, even when taking into account binding energy shifts due to (nano)cluster effects [24].

For V(TCNE)$_2$, the main peak at 6.5 eV and its high binding energy shoulder at 8 eV are mainly derived TCNE orbitals [13, 15]. Three features are present in the frontier valence region: the peaks are assigned to the destabilized highest occupied molecular orbital, HOMO (3.5 eV), and singly occupied molecular orbital, SOMO (1.5 eV) of $TCNE^-$, plus a hybridized V(3d)-TCNE ligand orbital at 1 eV, respectively [13, 15]. Though the number of peaks are the same in the frontier valence region for the two systems, the binding energies and the relative intensities differ, with the frontier peak in V(TCNE)$_x$ having the highest intensity unlike Fe(TCNE)$_x$ where the most intense peak is at

4.3 eV. The main peak and its high binding energy shoulders also differ in binding energy and relative intensities for $Fe(TCNE)_x$ and $V(TCNE)_x$. Hence, though qualitatively similar, the two valence spectra differ significantly, suggesting that the strength of metal–ligand interaction is dramatically different as well.

In order to probe the origin of the features in the $Fe(TCNE)_x$ valence spectrum, we have performed resonant photoelectron spectroscopy at the C K-edge, N K-edge, and Fe L_3-edge, presented in Figs. 3(a), (b), and (c), respectively. RPES is carried out by sweeping the photon energy in discrete steps over the respective absorption edge while detecting electrons emitted from the valence region. RPES hence will enhance features in the valence region originating from the element carrying the original (X-ray absorption-induced) core hole, allowing for "site-specific" analysis of the valence electronic structure. The RPES measurement series performed at the C K edge, N K-edge, and Fe L_3-edge all show some participator resonating behavior, i.e., the final state of the participator decay following the X-ray absorption has the same final state as for valence band PES enabling straightforward identification of the resonating features and correlation of them to the peaks and shoulders in Fig. 2 [13, 25]. Significant spectral weight also originates from a competing processes such as, e.g., spectator decay (peak binding energy increases linearly with increased photon energy) and Auger-like decay processes that appear as a background that increases with higher binding energies in the spectra.

The C K-edge RPES spectra (Fig. 3(a), left panel) were obtained by sweeping the photon energy from 280 to 288.4 eV in discrete steps so as to hit the peaks and shoulders in the C K-edge NEXAFS spectrum shown in Fig. 3(a), right panel. At 280 and 283.5 eV we are off-resonance, i.e., still below the absorption onset energy of the C K-edge for $Fe(TCNE)_x$, and hence no resonant behavior is seen. For 284.5 and 285.4 eV, the absorption onset has been passed, and there is a slight increase in the background intensity at higher binding energy, suggesting some resonant contribution to the signal. In the $h\nu = 286.5$ eV spectrum (C K-edge absorption maximum), however, we have several features in the valence band that show strong resonant enhancement, suggesting that they are mainly derived from orbitals on the TCNE units. Foremost is the resonant peak at 6.6 eV. Less obvious is the relative enhancement of the 3 and 1.7 eV features compared to the 4.5 eV feature, which causes a flattening of the region 1–5 eV. Similarly, the 8.8 eV feature is enhanced as compared to the ∼10 and ∼12 eV peaks in the valence band. The spectrum taken at 287.4 eV photon energy (second C K-edge absorption maximum) also shows strong resonance. Again, it is the main peak that is the strongest resonant feature, but here the center of the peak is shifted to higher binding energies, 7.3 eV, as compared to the nonresonant spectra. This shows that the main peak in the valence band is derived from at least two different molecular orbitals with significant electron density on carbon atoms in the TCNE groups, not surprising as TCNE has about 10 molecular orbitals in this region [26, 27]. Finally, the 288.4 eV is taken at the tail end of the main C K-edge π-absorption, and here the resonant effect is significantly weaker as expected and dominated by auger-type processes resulting in the large background.

RPES spectra were similarly obtained by scanning over the N K-edge NEXAFS region of $Fe(TCNE)_x$, see Fig. 3(b). Again, the spectra taken below the N K-edge absorption onset (390 and 394 eV) show no resonant effects. At 398.0 eV we are sitting at the center of the (weak) onset of the absorption feature, and the valence region spectrum shows resonating behavior as evident from the increased background. The 399.4 eV photon energy RPES spectrum corresponds to the main absorption peak of the N K-edge spectrum, and strong resonant enhancement is seen for the features located at ∼6.4 and ∼8.6 eV, and, as for the C K-edge RPES, the relative flattening out of the 1–5 eV region suggests resonant enhancement of the 1.7 and 3 eV features as compared to the 4.5 eV feature. The spectrum taken at 400.5 eV (second absorption maximum) shows strong resonant behavior, but here the dominant effect is the increase of the background due to Auger-type processes. Two resonating peaks are located at 8.6 and 9.8 eV, and again there is resonant enhancement of the 1.7 and 3 eV features as compared to the 4.5 eV feature in the frontier valence region. The two high binding energy resonant peaks appear at binding energies higher than for the 399.4 eV RPES spectrum. This could be interpreted as a linear shift with the increased photon energy (6.4 to 8.6 eV, 8.6 to 9.8 eV) due to spectator decay [25] but also may be a result of new molecular orbitals coming in resonance upon change in photon energy, and/or effects related to specifically enhanced vibrational states [28].

The RPES spectra for the Fe L_3-edge are presented in Fig. 3(c). The second-order light contribution is very weak and does significantly affect even the off-resonance spectra, unlike the case for the C and N K-edge spectra, so background subtraction of this feature was not necessary. At 705.9 eV, the onset of absorption has just been crossed, and the peak at ∼4.5 eV shows some enhancement, suggesting resonant behavior. At $h\nu = 707.9$ eV we are at the absorption maximum and we can see strong resonant enhancement of the 4.5 eV feature, now shifted to slightly higher binding energy. This suggests that this feature has its origin in Fe(3d)-derived orbitals. Based on the combined PES and RPES results, we can thus assign the first two frontier peaks (HOMO, HOMO-1) in the valence region of $Fe(TCNE)_x$ to be mainly TCNE-derived and the third peak (HOMO-2) to be mainly Fe(3d) derived, in stark contrast to the case for $V(TCNE)_2$.

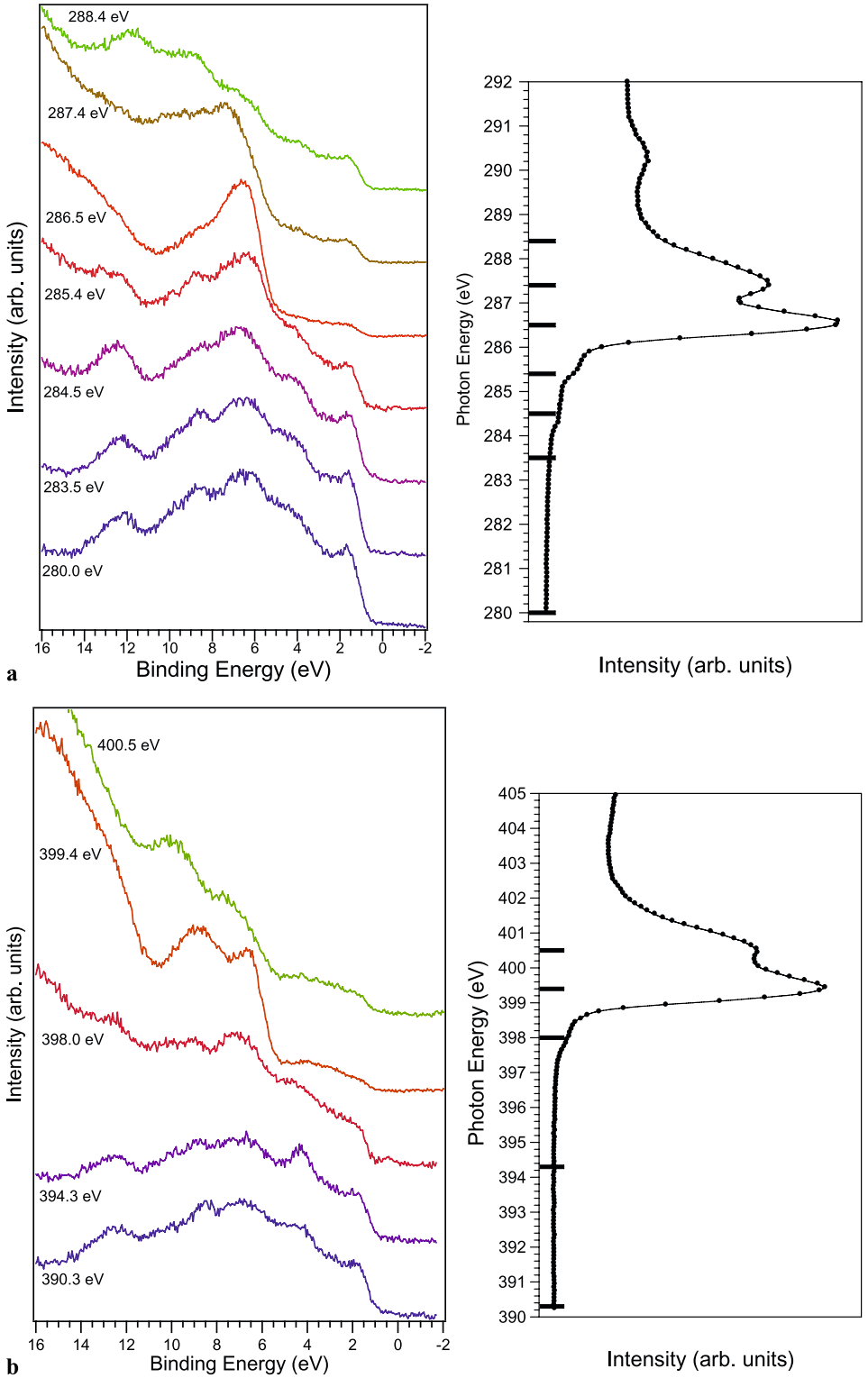

Fig. 3 **a** *Left panel*: RPES spectra taken by sweeping the photon energy over the C K-edge. The second-order light-induced C(1s) core level peak feature has been subtracted from the spectra. The intensities of the individual spectra have been adjusted so as to fit the scale of the figure. *Right panel*: the corresponding C K-edge NEXAFS spectrum. The RPES photon energies used are represented as black bars. **b** *Left panel*: RPES spectra taken by sweeping the photon energy over the N K-edge. The second-order light-induced N(1s) core level peak feature has been subtracted from the spectra. The intensities of the individual spectra have been adjusted so as to fit the scale of the figure. *Right panel*: the corresponding N K-edge NEXAFS spectrum. The RPES photon energies used are represented as *black bars*. **c** *Left panel*: RPES spectra taken by sweeping the photon energy over the Fe L_3-edge. The intensities of the individual spectra have been adjusted so as to fit the scale of the figure. *Right panel*: the corresponding Fe L_3-edge XAS spectrum. The RPES photon energies used are represented as *black bars*

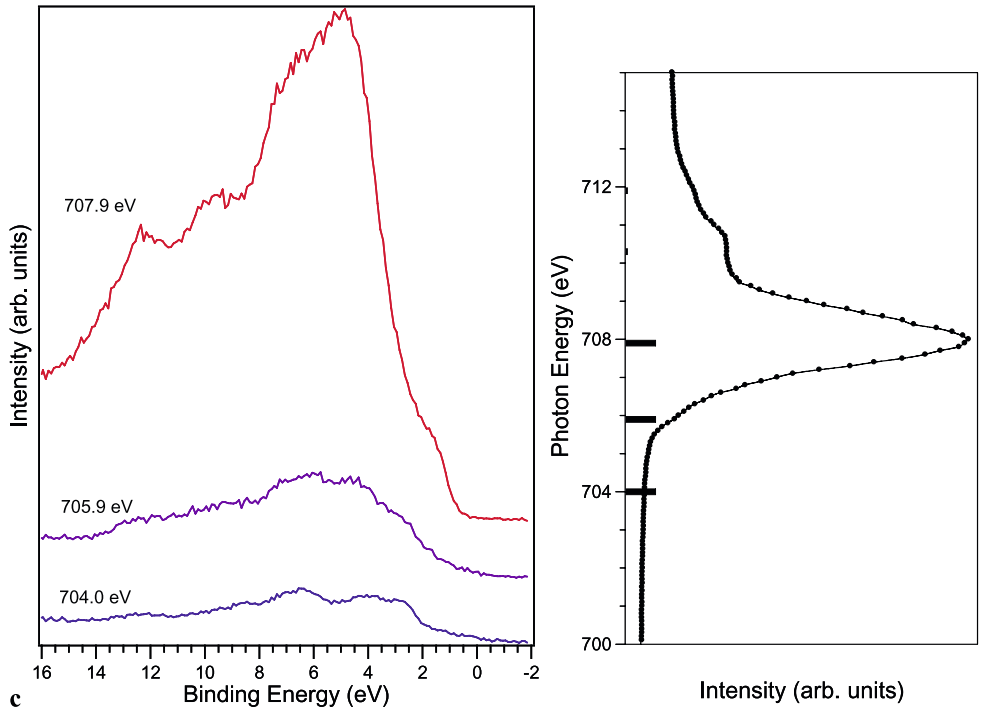

Fig. 3 (Continued)

The Fe L-edge XAS spectrum is presented in Fig. 4, top spectrum (blue line). A small linear background has been subtracted from the data to allow for easier comparison with calculations. The Fe L-edge XAS spectrum is composed of a number features arising from electric dipole transitions between the Fe(2p) core level and empty Fe(3d) valence states, while additional contributions of Fe(2p) $\rightarrow$ Fe(4s) transitions are negligible. The two main features in the spectra correspond to two groups of multiplets involving Fe($2p_{3/2}$) (L_3-edge, peak centered at 707.9 eV) and Fe($2p_{1/2}$) (L_2-edge, peak centered at 720.8 eV) states, respectively, separated by the Fe(2p) spin orbit coupling energy. Due to the strong interaction between the Fe(2p) core holes and the Fe(3d) valence electrons, the excited states remain strongly localized on the Fe-ions. Consequently, the Fe L-edge NEXAFS spectrum of Fe(TCNE)$_x$ is expected to be closely related to the atomic multiplet structure, allowing accurate description of experiments by ligand field multiplet (LFM) calculations. Three electronic configurations were first tried in the LFM calculations: d^6 (Fe^{2+}), d^5 (Fe^{3+}), and d^4 (Fe^{4+}) for several different values of the octahedral crystal field between 0 and 2 eV. The high-spin d^6 ($10Dq < 1.8$ eV) configuration provided by far the best fit to the experimental spectrum, confirming the Fe^{2+} assignment from the PES results. This is in agreement with earlier results, where Mössbauer spectroscopy of Fe(TCNE)$_2 \cdot y(CH_2Cl_2)$ showed that iron in that compound is divalent and high spin ($S = 2$) [29]. The calculated spectra for Fe^{2+} (d^6) with $10Dq = 0$, 0.5, 1.0, 1.5, and 2.0 eV are shown in the bottom panel of Fig. 4. The spectra are shifted on the photon energy scale to match the measurement (note that the calculations do not give reliable absolute values of the excitation energies). The Slater integrals are scaled to 80% of their atomic values to compensate for solid state effects (expansion of the electron clouds as compared to the isolated ion). Further downscaling, which is typically used to mimic the nephelauxetic effects resulting from covalency, did not produce better agreement with the experiment. The discrete excitation energy values were broadened with Gaussians (0.4 eV) plus Lorentzians to account for experimental resolution, vibrational broadening, and lifetime broadening. A Lorentzian broadening of 0.1 eV was used for the L_3-edge, while this value was increased to 0.5 eV for the L_2-edge to simulate the reduced lifetime of the $2p_{1/2}$ core holes due to the availability of Coster–Kronig decay channels. Clearly, the agreement with experiment is best for relatively small values of the crystal field parameter. Note that a high-spin to low-spin transition occurs as $10Dq$ varies from 1.5 to 2.0 eV, so that the 2.0 eV spectrum corresponds to the low-spin d^6 configuration ($S = 0$). After performing a more detailed series of calculations, in which the crystal field strength was varied $10Dq$ in finer steps, the best fit was obtained for a crystal field parameter $10Dq = 0.6$ eV, shown in the top panel of Fig. 4 (red line). A set of CTM calculations (not shown) were tried as

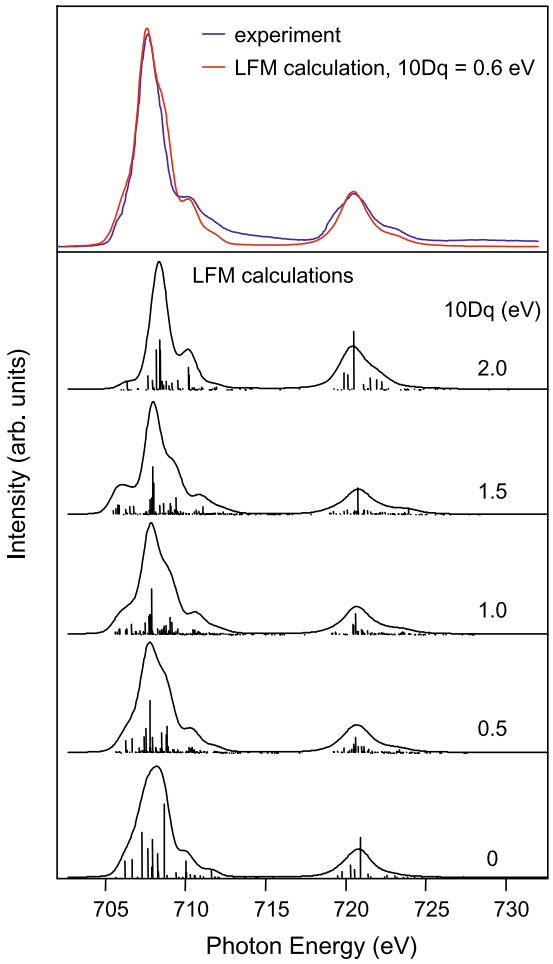

Fig. 4 Fe L-edge XAS spectrum (*top panel, blue*) plus simulated spectra obtained by LFM calculations. The *bottom panel* contains calculated spectra plus *vertical bars* indicating the discrete energy states for different values of the octahedral crystal field parameter $10Dq$ between 0 and 2 eV. The best agreement with the experimental data was obtained for an LFM calculation with $10Dq = 0.6$ eV (*top panel, red*). Further details are given in the text

well, but inclusion of TCNE-to-iron electron transfer does not improve the fit, as the CT creates satellites between the Fe L_3- and L_2-edges, which is not observed in the experimental spectrum in Fig. 4. These results are in sharp contrast to V(TCNE)$_x$, $x \sim 2$, where the crystal field is substantially larger ($10Dq = 2.3$ eV), and the combined LFM and CTM calculations yield a hybrid V($3d$)-CN ground state given by 60% $3d^3$ and 40% $3d^4\underline{L}$, where $\underline{L}$ is a hole on the TCNE (cyano) ligands [15]. The weaker Fe-TCNE ligand interaction as compared to V-TCNE and the drastically different frontier valence electronic structure may help explain the substantially lower magnetic ordering temperature ($T_C = 97$ K) for Fe(TCNE)$_x$-type magnets [30] than that for V(TCNE)$_x$ ($T_C \sim 400$ K).

4 Summary and conclusions

Thin film Fe(TCNE)$_x$, $x \sim 2$, was grown in situ under ultra-high vacuum conditions using a recently developed PVD-based technique for fabrication of oxygen- and precursor defect-free organic-based molecular magnets. No spurious trace elements were found in the films, and the iron was of Fe^{2+} valency. The highest occupied molecular orbital of Fe(TCNE)$_x$ is located at ~1.7 eV vs. Fermi level and is derived mainly from the TCNE- singly occupied molecular orbital according to photoelectron spectroscopy and resonant photoelectron spectroscopy results. The Fe(3d)-derived states appear at higher binding energy, ~4.5 eV, which is in contrast to V(TCNE)$_2$, where the highest occupied molecular orbital is mainly derived from V(3d) states. Fitting LFM and CTM calculations to the Fe L-edge NEXAFS spectrum yielded a high-spin Fe^{2+} ($3d^6$) configuration with a crystal field parameter $10Dq \sim 0.6$ eV for the Fe(TCNE)$_x$ system. We propose that the weaker Fe-TCNE ligand interaction as compared to V(TCNE)$_2$ and the drastically different frontier valence electronic structure are strongly contributing factors to the substantially lower magnetic ordering temperature (T_C) seen for Fe(TCNE)$_x$-type magnets.

Acknowledgements The authors acknowledge financial support from the Swedish Research Council (VR), the Carl Tryggers Foundation, The Knut and Alice Wallenberg Foundation, and the Swedish Foundation for Strategic Research funded Center for Advanced Molecular Materials, CAMM.

References

1. J.M. Manriquez, G.T. Yee, R.S. McLean, A.J. Epstein, J.S. Miller, Science **252**, 1451 (1991)
2. M.A. Girtu, in *Magnetic Nanostructures*, ed. by H.S. Nalwa (Am. Sci., Los Angeles, 2002), pp. 359–405. ISBN 1-58883-000-4
3. J.S. Miller, Inorg. Chem. **29**, 4392 (2000)
4. B.G. Morin, C. Hahm, A.J. Epstein, J.S. Miller, J. Appl. Phys. **75**, 5782 (1994)
5. A.J. Epstein, B.G. Morin, United States Patent 5,821,453
6. A.J. Epstein, V.N. Prigodin, United States Patent 6,621,100
7. D. de Caro, M. Basso-Bert, J. Sakah, H. Casellas, J.-P. Legros, L. Valade, P. Cassoux, Chem. Mater. **12**, 587 (2000)
8. K.I. Pokhodnya, A.J. Epstein, J.S. Miller, Adv. Mater. **12**, 410 (2000)
9. D. de Caro, C. Faulmann, L. Valade, Chem. Eur. J. **13**, 1650 (2007)
10. M.S. Thorum, K.I. Pokhodnya, J.S. Miller, Polyhedron **25**, 1927 (2006)
11. P. Zhou, S.M. Long, J.S. Miller, A.J. Epstein, Phys. Lett. A **181**, 71 (1993)
12. K.I. Pokhodnya, D. Pejakovic, A.J. Epstein, J.S. Miller, Phys. Rev. B **63**, 174408 (2001)
13. C. Tengstedt, M.P. de Jong, A. Kanciurzewska, E. Carlegrim, M. Fahlman, Phys. Rev. Lett. **96**, 057209 (2006)
14. E. Carlegrim, A. Kanciurzewska, P. Nordblad, M. Fahlman, Appl. Phys. Lett. **92**, 163308 (2008)
15. M.P. de Jong, C. Tengstedt, A. Kanciurzewska, E. Carlegrim W, R. Salaneck, M. Fahlman, Phys. Rev. B **75**, 064407 (2007)

16. E. Carlegrim, B. Gao, A. Kanciurzewska, M.P. de Jong, Z. Wu, Y. Luo, M. Fahlman, Phys. Rev. B **77**, 054420 (2008)
17. E. Carlegrim, A. Kanciurzewska, M.P. de Jong, C. Tengstedt, M. Fahlman, Chem. Phys. Lett. **452**, 173 (2008)
18. B.T. Thole, G. Van Der Laan, P.H. Butler, Chem. Phys. Lett. **149**, 295 (1988)
19. K. Okada, A. Kotani, B.T. Thole, J. Electron Spectrosc. Relat. Phenom. **58**, 325 (1992)
20. K. Okada, A. Kotani, H. Ogasawara, Y. Seino, B.T. Thole, Phys. Rev. B **47**, 6203 (1993)
21. R.D. Cowan, *The Theory of Atomic Structure and Spectra* (University of California Press, Berkeley, 1981)
22. P.H. Butler, *Point Group Symmetry Applications: Methods and Tables* (Plenum, New York, 1981)
23. C.D. Wagner, in *Practical Surface Analysis*, vol. 1, 2nd edn., ed. by D. Briggs, M.P. Seah (Wiley, New York, 1990), ISBN 0-471-92081-9
24. M.A. Hoffmann, G. Wrigge, B. von Issendorff, Phys. Rev. B **66**, 041404(R) (2002)
25. P.A. Brühwiler, O. Karis, N. Mårtenson, Rev. Mod. Phys. **74**, 703 (2002)
26. V.G. Zakrzewski, O. Dolgounitcheva, J.V. Ortiz, J. Chem. Phys. **105**, 5872 (1996)
27. K.N. Houk, L.L. Munchausen, J. Am. Chem. Soc. **98**, 937 (1976)
28. R. Friedlein, S.L. Sorensen, A. Baev, F. Gel'mukhanov, J. Birgerson, A. Crispin, M.P. de Jong, W. Osikowicz, C. Murphy, H. Ågren, W.R. Salaneck, Phys. Rev. B **69**, 125204 (2004)
29. J. Zhang, J. Ensling, V. Ksenofontov, P. Gutlich, A.J. Epstein, J.S. Miller, Angew. Chem. Int. Ed. Engl. **37**, 657 (1998)
30. M.A. Girtu, C.M. Wynn, J. Zhang, J.S. Miller, A.J. Epstein, Phys. Rev. B **61**, 492 (2000)